nature chemistry

Article

https://doi.org/10.1038/s41557-023-01268-0

Triarylmethyl cation redox mediators enhance Li–O_2 battery discharge capacities

Received: 3 April 2022

Accepted: 6 June 2023

Published online: 06 July 2023

Check for updates

Erik J. Askins[1,2], Marija R. Zoric[3], Matthew Li[2], Rachid Amine[4], Khalil Amine[2], Larry A. Curtiss[4] & Ksenija D. Glusac[1,2]

A major impediment to Li–O_2 battery commercialization is the low discharge capacities resulting from electronically insulating Li_2O_2 film growth on carbon electrodes. Redox mediation offers an effective strategy to drive oxygen chemistry into solution, avoiding surface-mediated Li_2O_2 film growth and extending discharge lifetimes. As such, the exploration of diverse redox mediator classes can aid the development of molecular design criteria. Here we report a class of triarylmethyl cations that are effective at enhancing discharge capacities up to 35-fold. Surprisingly, we observe that redox mediators with more positive reduction potentials lead to larger discharge capacities because of their improved ability to suppress the surface-mediated reduction pathway. This result provides important structure–property relationships for future improvements in redox-mediated O_2/Li_2O_2 discharge capacities. Furthermore, we applied a chronopotentiometry model to investigate the zones of redox mediator standard reduction potentials and the concentrations needed to achieve efficient redox mediation at a given current density. We expect this analysis to guide future redox mediator exploration.

The Li–oxygen battery exhibits a tremendously high theoretical specific energy and is receiving interest as a next-generation energy system. In a typical cell, O_2 is reduced through a series of Li^+-coupled electron-transfer steps or disproportionation to grow Li_2O_2 (refs. 1,2). Although the Li–O_2 battery promises large energy density and capacities, the extent to which it can deliver on this promise is contingent upon the mechanisms by which solid Li_2O_2 growth is mediated. After its initial reduction at the carbon cathode, subsequent steps involving LiO_2 intermediates may proceed in different locations. For example, in one case, LiO_2 may stay on the electrode surface and be reduced to Li_2O_2, generating a thin layer of Li_2O_2, which electronically passivates the electrode, resulting in premature cell death[1,3]. Alternatively, LiO_2 may dissolve into the electrolyte and, through disproportionation, generate Li_2O_2 away from the electrode, delivering large battery capacities. With normal Li–O_2 electrolytes (additive-free, non-polar organic solvents), the solubility of reduced oxygen intermediates is low, and the electrode-mediated process dominates. Therefore, it is paramount to control the oxygen reduction reaction (ORR) pathway and drive it into solution.

To boost the solution-based mechanism of Li_2O_2 formation in Li–O_2 batteries, polar species[4–7] and redox-active compounds were tested as additives[8–16]. These additives move the Li_2O_2 formation site from the electrode surface into solution, but their mechanism of action varies. Polar species increase the solubility of Li^+ or LiO_2 intermediates but are understood to negatively impact long-term cyclability[7]. A more effective approach is redox mediation, wherein small molecules shuttle electrons from the electrode to O_2. Quinone-based redox mediators promote solution discharge via an inner-sphere mechanism involving an oxygen–quinone intermediate formed by reaction between reduced quinone and O_2 (refs. 8–10,12,13). Li–O_2 batteries with quinone-based additives have achieved up to 100-fold capacity improvement[9] and exhibited toroidal Li_2O_2 formation on the electrode, indicating solution-phase growth[17]. Outer-sphere redox mediation has also been explored with viologen derivatives, which

[1]Department of Chemistry, University of Illinois Chicago, Chicago, IL, USA. [2]Chemical Sciences and Engineering Division, Argonne National Laboratory, Lemont, IL, USA. [3]Stanford PULSE Institute, SLAC National Accelerator Laboratory, Menlo Park, CA, USA. [4]Material Science Division, Argonne National Laboratory, Lemont, IL, USA. e-mail: glusac@uic.edu

https://doi.org/10.1038/s41557-023-01268-0

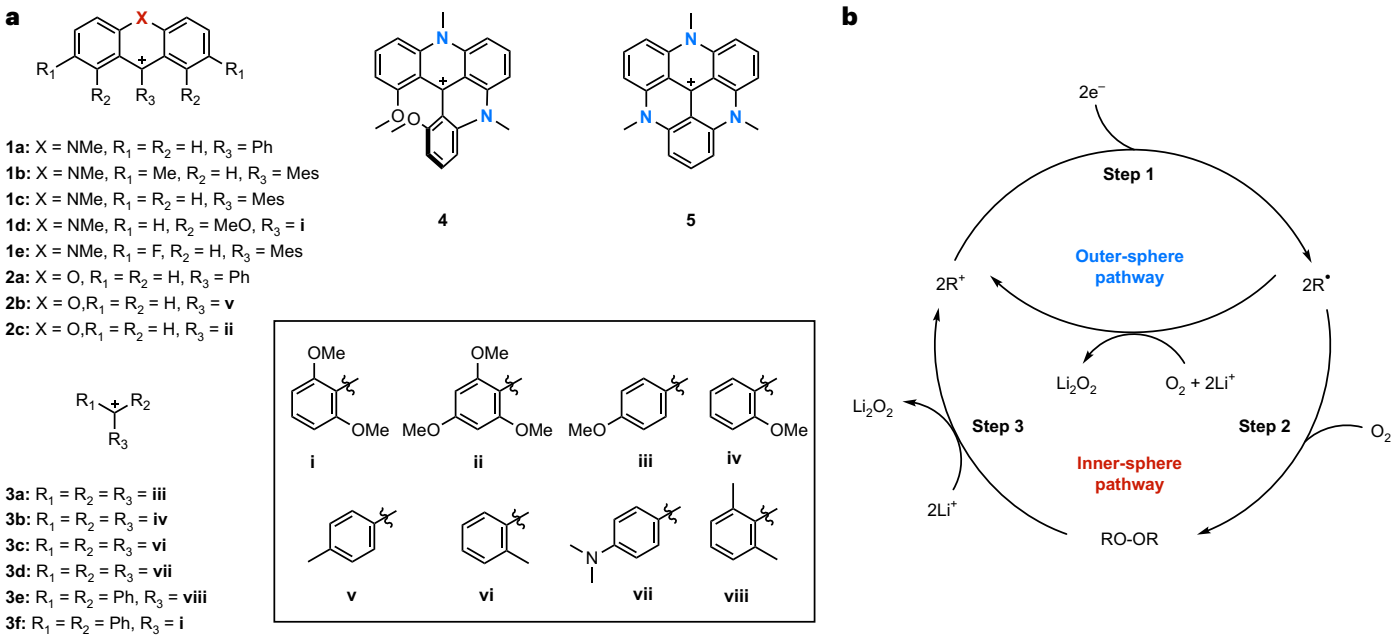

Fig. 1 | Chemical structures and proposed mechanistic overview of triarylmethy cation redox mediation. a, Structures of triarylmethyl cations from the triphenylmethyl, acridinium and xanthylium families. **b**, Mechanistic overview of the inner-sphere (peroxide formation) and outer-sphere (redox mediation) pathways.

serve as electron shuttles that facilitate superoxide formation away from the electrode[14,15]. Additionally, non-redox-active catalysts, based on the biomimetic catalytic disproportionation of superoxide into O_2 and peroxide[16], have recently been investigated.

Once discharged, recharging the battery presents itself as another performance-limiting hurdle for Li–O_2 batteries. Large overpotentials are required to oxidize Li_2O_2 deposits. At such oxidizing potentials, cell components such as the solvent and carbon electrode are susceptible to degradation. Redox mediation is again an effective strategy to address these concerns. Here, redox mediation proceeds through oxidation of the mediator at the electrode at low overpotentials. Oxidized mediators deliver an electron hole needed for Li_2O_2 oxidation. Several inorganic anions have been introduced as charging redox mediators (I^-, Br^- and NO_3^-)[18–20]. However, the inability to tune oxidation potentials and the negative effects on battery efficiency have led researchers to explore organic compounds for charge redox mediation[11,18,19,21–25]. The nitroxyl-based (2,2,6,6-tetramethylpiperidin-1-yl)oxyl (TEMPO) demonstrated the best performance and stability. Indeed, when joint 2,5-di-*tert*-butyl-1,4-benzoquinone (DBBQ)/TEMPO discharge/charge redox mediators are used, long-term stability has been achieved, suggesting that joint redox mediators are a viable path towards a highly efficient and long-cycling Li–O_2 battery[26].

Despite the progress made with redox mediators, their lack of chemical diversity has prevented further developments in the field. For example, most discharge mediators are quinone-based, and a large number of compounds from this family have been explored. Following our group's interest in redox-active organic compounds as catalysts in electrochemistry[27–35], we now investigate an unexplored type of discharge mediator for Li–O_2 batteries, based on triarylmethyl cation motifs (Fig. 1a). Density functional theory (DFT) screening was used to evaluate the thermodynamic parameters that control inner-sphere and outer-sphere catalysis mechanisms for O_2/Li_2O_2 reduction by the triarylmethyl cations under study. Cyclic voltammetry (CV) revealed substantial catalytic activity for a selection of outer-sphere redox mediators, with the fastest catalysis resulting from more negative reduction potentials ($E_{R^+/R^\bullet}$). When tested for their effect on Li–O_2 discharge capacity, enhancements of up to 35-fold were seen, which is competitive with the best reported quinone-based mediators. Interestingly, larger capacities resulted from mediators with sluggish catalytic rates (more positive $E_{R^+/R^\bullet}$), because of their ability to maintain more positive cell potentials and effectively suppress surface-mediated O_2 reduction. Complementary chronopotentiometry modelling revealed that redox mediation can be achieved for mediators with reduction potentials more positive than what has been explored. This work introduces a family of highly active redox mediators and reveals the important criteria for designing future redox mediators with more positive potentials and high concentrations for further improvement to Li–O_2 battery discharge lifetimes.

Results and discussion

Model compounds

The triarylmethyl cations (R^+) investigated here consist of acridinium (compounds **1a**–**e**, **4** and **5**), xanthylium (compounds **2a**–**c**) and triphenylmethyl (compounds **3a**–**f**) frameworks, as shown in Fig. 1a (their synthesis is described in the Methods). The structural diversity of R^+ comes from the introduction of heteroatoms, such as N or O, directly into the conjugated motifs, and substitution on aryl rings with electron-withdrawing and -donating groups. Two plausible oxygen reduction catalysis mechanisms were explored, namely the outer- and inner-sphere pathways (Fig. 1b). Both mechanisms are initiated by one-electron reduction of R^+ to form a neutral radical ($R^\bullet$), so the catalytic overpotential is directly related to the standard reduction potential $E^0(R^+/R^\bullet)$. Our cations appear ideal for this type of reactivity, because their $E^0(R^+/R^\bullet)$ values are situated near the O_2/Li_2O_2 couple (2.96 V)[30,35–37]. Furthermore, the $E^0(R^+/R^\bullet)$ values were tailored to suit redox mediation by substitution with electron-donating and -withdrawing groups, which shift $E^0(R^+/R^\bullet)$[30,37,38]. For efficient redox mediation, $R^\bullet$ must be stable and persistent in the electrolyte solution. Although organic radicals often deactivate via radical–radical dimerization[39], our neutral radicals are stable because of radical spin delocalization across their conjugated cores and the presence of sterically bulky phenyl substituents that prevent radical–radical dimerization[40]. This was confirmed by computing dimerization energies for a subset of neutral radicals (Supplementary Section 2). In the outer-sphere pathway, $R^\bullet$ reduces O_2 via homogeneous electron transfer, regenerating cationic R^+, while the inner-sphere mechanism involves reaction of $R^\bullet$ with O_2 to form the peroxide RO–OR

https://doi.org/10.1038/s41557-023-01268-0

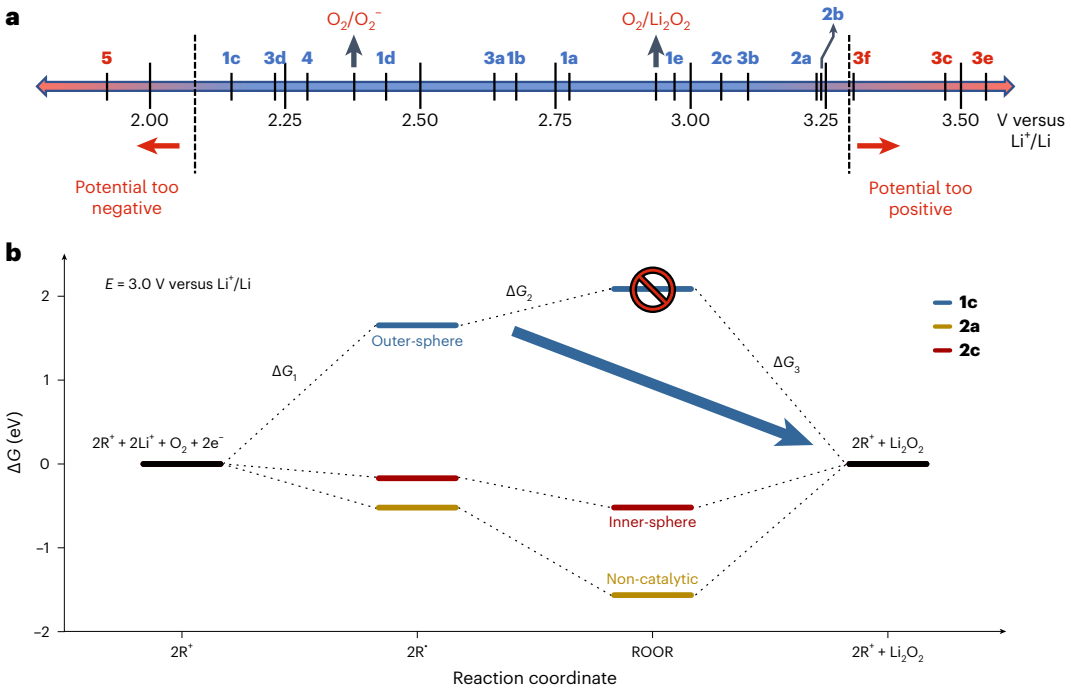

Fig. 2 | Computational screening of redox mediators. a, DFT-computed $R^+/R^•$ standard reduction potentials for each redox mediator candidate, along with the potential for O_2/O_2^- reduction and the thermodynamic potential for the overall O_2/Li_2O_2 reaction[42]. Redox mediator candidates listed in blue have desirable reduction potentials and are within the window of 2.10–3.26 V. **b**, Energy diagram for selected redox mediators that are predicted to exhibit different behaviour: **1c** (ΔG_2^0 is uphill, outer-sphere redox mediation), **2c** (ΔG_3^0 is mildly uphill, inner-sphere catalysis) and **2a** (ΔG_3^0 is highly uphill, non-catalytic).

(Fig. 1b). Some $R^•$ in Fig. 1a have been shown to react rapidly with O_2 to form RO–OR[36], which prompted us to investigate this mechanistic pathway. Catalytic cycle closure in the inner-sphere pathway is achieved by the formation of Li_2O_2 through reaction of RO–OR with Li^+.

Computational screening

Thermodynamic evaluations of the inner- and outer-sphere mechanisms were performed at the DFT level of theory by calculating ΔG^0 values for the formation of $R^•$ (ΔG_1^0; Fig. 1b, step 1), the reaction between $R^•$ and O_2 (ΔG_2^0, step 2), and the reaction between RO–OR and Li^+ (ΔG_3^0, step 3). Computational details, including free-energy calculations and an explanation of the screening criteria, are provided in Supplementary Section 2. Using calculated $E^0(R^+/R^•)$ and ΔG^0 values, we constructed a flowchart that predicts the activity of proposed cations as inner- or outer-sphere redox mediators (Supplementary Scheme 1).

Step 1 compares $E^0(R^+/R^•)$ with an established electrochemical window for oxygen catalysis (2.96–2.40 V) based on the standard reduction potentials for O_2/Li_2O_2 (ref. 41) and O_2/O_2^- (ref. 42) conversion, respectively. An additional ±0.30-V allowance was applied to the window to account for inaccuracies in the DFT. These potentials are marked on the potential scale in Fig. 2a with calculated $E^0(R^+/R^•)$ values. Calculated $E^0(R^+/R^•)$ values match the experimentally observed $E_{R+/R•}$ values well (Supplementary Table 6). As expected, $E^0(R^+/R^•)$ shifted to more positive potentials with the introduction of electron-withdrawing heteroatoms (for example, oxygen or nitrogen) or substituents (for example, fluorine) and more negative potentials with electron-donating substituents (for example, methoxy). As such, compounds **3c**, **3e**, **3f** and **5** were removed based on their $E^0(R^+/R^•)$ values being outside the established potential window.

The ΔG_2^0 and ΔG_3^0 values indicate the likelihood of the inner-sphere reaction with O_2 and subsequent closure of the catalytic cycle (Supplementary Table 6). Positive ΔG_2^0 values (**1b**, **1c**, **1d**, **1e**, **2b** and **4**) suggest that the inner-sphere reaction with O_2 is non-spontaneous. The steric bulk imparted by substituted phenyl rings at the C9 positions of each of these compounds restricts access to the tertiary carbon-centred radical. These cations were viewed as candidates for the outer-sphere process and were evaluated using CV. For compounds with negative ΔG_2^0 values (**1a**, **2a**, **2c**, **3a**, **3b** and **3d**), formation of RO–OR through the inner-sphere pathway is expected to be spontaneous. Here, ΔG_3^0 values reflect the feasibility of RO–OR reacting with Li^+ and regenerating R^+. Highly positive ΔG_3^0 values suggest that **1a**, **2a** and **3a** form stable peroxides incapable of reaction with Li^+, and so they were removed as candidates. Conversely, the electron-donating substituents of **2c**, **3b** and **3d** decrease the acidity of R^+, making a less stable RO–OR and providing mild ΔG_3^0 values, making them suitable candidates for inner-sphere redox mediation.

Figure 2b illustrates how calculated thermodynamic parameters affect redox mediation mechanisms. Three organic cations expected to perform redox mediation, via the inner- or outer-sphere mechanisms (compounds **1c** and **2c**, respectively), or be catalytically inactive (compound **2a**) are shown. The diagram, presented at an applied potential of 3.0 V, shows anticipated overpotentials for each process. All three mediators exhibit positive or mildly negative ΔG_1^0 values. The positive ΔG_2^0 for **1c** indicates that RO–OR is unlikely, instead favouring the outer-sphere mechanism. In contrast, the negative ΔG_2^0 values of **2a** and **2c** suggest the spontaneous inner-sphere reaction with O_2. ΔG_3^0 differentiates **2a** and **2c**. ΔG_3^0 is highly positive for **2a**, indicating that the RO–OR is stable and will not react with Li^+. Thus **2a** is expected to be non-catalytic. ΔG_3^0 is only mildly positive for **2c**, suggesting that it may reasonably function as an inner-sphere redox mediator. Based on these criteria, cations **1b**, **1c**, **1d**, **1e**, **2b**, **2c**, **3b**, **3d** and **4** are viewed as promising candidates for discharge redox mediation in Li–O_2 batteries via the inner- or outer-sphere mechanism (Supplementary Table 6).

Cyclic voltammetry

Redox mediation candidates were investigated with CV in Li^+-containing Ar- and O_2-saturated tetraethylene glycol dimethyl ether (TEGDME) solutions (Fig. 3 and Supplementary Fig. 1). In the absence of O_2,

https://doi.org/10.1038/s41557-023-01268-0

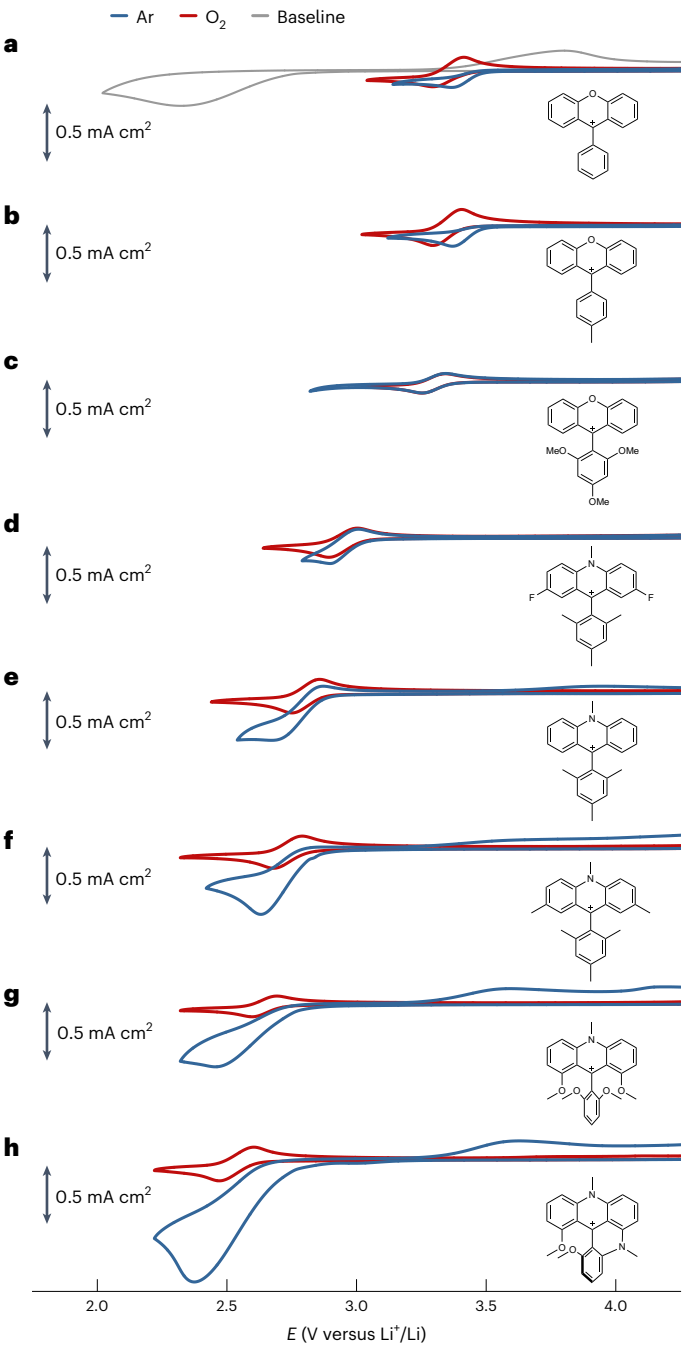

Fig. 3 | Cyclic voltammograms of various redox mediators. CVs of redox mediators in Ar- (red trace) and O_2-saturated (blue trace) electrolyte and redox mediator-free solutions (grey). **a**–**h**, The CVs are organized in order of descending $E_{R^+/R^\cdot}$ beginning with **2a** (**a**), **2b** (**b**), **2c** (**c**), **1e** (**d**), **1c** (**e**), **1b** (**f**), **1d** (**g**) and **4** (**h**). The CVs were recorded in TEGDME containing 1 M lithium triflate (LiOTF) and 3 mM redox mediator at a scan rate of 100 mV s^{-1}.

a single chemically reversible $R^+/R^\cdot$ reduction was observed for all R^+ cations, which are plotted in order of decreasing potentials. Generally, $E_{R^+/R^\cdot}$ is within ±0.2 V of the DFT-calculated values (Supplementary Table 6) and their trends are rationalized using electronic effects described in the previous section. Several behaviours were observed in the presence of O_2. In one case, the $R^+/R^\cdot$ peak of **2c** (Fig. 3c) was largely unaffected by O_2, signalling that there is no follow-up reaction between $R^\cdot$ and O_2 on our CV timescales. The highly positive $E_{R^+/R^\cdot}$ of **2c** made $R^\cdot$ insufficiently reducing to facilitate electron transfer to O_2 or formation of RO–OR. However, this behaviour is limited to the kinetic window of CV measurements, and the inner-sphere behaviour of **2c** may operate on longer timescales.

In the case of **2a** and **2b** (Fig. 3a,b), cathodic $R^+/R^\cdot$ features shift to more positive potentials and anodic peaks disappear, consistent with successive electrochemical and chemical steps (EC-type mechanism), wherein $R^+/R^\cdot$ reduction is followed by reaction with O_2, forming RO–OR through the inner-sphere pathway. The presence of an irreversible oxidation feature in the anodic scan, corresponding to RO–OR oxidation, was evidence for RO–OR formation (Supplementary Fig. 2)[36]. Lack of catalytic current enhancement to $R^+/R^\cdot$ reduction suggests that **2a** and **2b** terminally formed RO–OR and no follow-up reaction with Li^+ occurred. As confirmation, chemically and electrochemically derived RO–OR species **2a**/RO–OR and **2b**/RO–OR were prepared. Both derivatives show the same UV–vis results lacking the broad absorption between 350 and 500 nm of their R^+ precursors (**2a** and **2b**; Supplementary Fig. 2). Adding Li^+ to solutions of **2a**/RO–OR and **2b**/RO–OR showed no recovery of the UV–vis signatures of **2a** and **2b**, leading us to conclude that **2a** and **2b** are non-catalytic. Although **2a** and **2b** did not show any inner-sphere catalysis, it remains plausible that other redox mediators, with appropriate $E_{R^+/R^\cdot}$ and that form less stable peroxides, will exhibit inner-sphere catalysis.

Compounds with the highest degree of catalytic enhancement came from the family of acridinium-based redox mediators, which were all predicted to function through the outer-sphere mechanism (**1e**, **1c**, **1b**, **1d** and **4**). Their CVs are shown in Fig. 3d–h and are characterized by taking **1c** (Fig. 3e) as an example: in the presence of O_2, $R^+/R^\cdot$ reduction shifts to more positive potentials, becomes chemically irreversible, and experiences a marked current enhancement. The credibility of the predicted outer-sphere mechanism was examined by a series of CV experiments on **1c** based on Savéant's work on outer-sphere (redox) catalysis[43,44]. These results are detailed in Supplementary Fig. 3 and Supplementary Table 1.

Interestingly, outer-sphere redox mediation was only observed in the presence of Li^+. The redox behaviours of **1c** in Li^+-free $TBAPF_6$ and Li^+-containing $TBAPF_6$ electrolytes are shown in Supplementary Fig. 4. In Ar-saturated environments, reversible $R^+/R^\cdot$ reduction is seen at 2.80 V in both electrolytes, so Li^+ does not influence $R^+/R^\cdot$ reduction. However, in O_2-saturated, Li^+-free electrolyte, no catalytic enhancement is observed. Instead, separate $R^+/R^\cdot$ and O_2/O_2^- redox waves are present at 2.80 and 2.40 V, respectively, suggesting that the second step in the outer-sphere pathway, homogeneous electron transfer between $R^\cdot$ and O_2, is Li^+-coupled. This type of ion-coupled catalysis, commonly seen in many proton-coupled processes[45], is sparsely reported in the Li–O_2 field[46]. We are currently investigating the role of Li^+ in catalysis, but we expect that large Li^+ concentrations generate the driving force for Li^+ to pre-associate O_2 and form an $Li^+\cdots O_2$ adduct that participates in the outer-sphere redox mediation.

To better understand the outer-sphere redox mediation, rate constants associated with the electrochemical and chemical steps were estimated. The experimental data were simulated using the following electrochemical and chemical steps (Supplementary Section 1 provides more information):

$$R^+ + e^- \rightleftarrows R^\cdot \quad k_1 \tag{1}$$

$$R^\cdot + Li^+ \cdots O_2 \rightleftarrows R^+ + LiO_2 \quad K_{eq,2},\ k_2,\ k_{-2} \tag{2}$$

Where k_1 is the heterogeneous electron transfer rate constant which ranged from 0.0098 to 0.012 cm s^{-1}, confirming fast electron transfer between the electrode and redox mediators. The resulting bimolecular rate constants for reaction between $R^\cdot$ and $Li^+\cdots O_2$ (k_2) are plotted with respect to $E_{R^+/R^\cdot}$ in Supplementary Fig. 8. Noticeably, the level of catalytic enhancement increases as $E_{R^+/R^\cdot}$ becomes more

https://doi.org/10.1038/s41557-023-01268-0

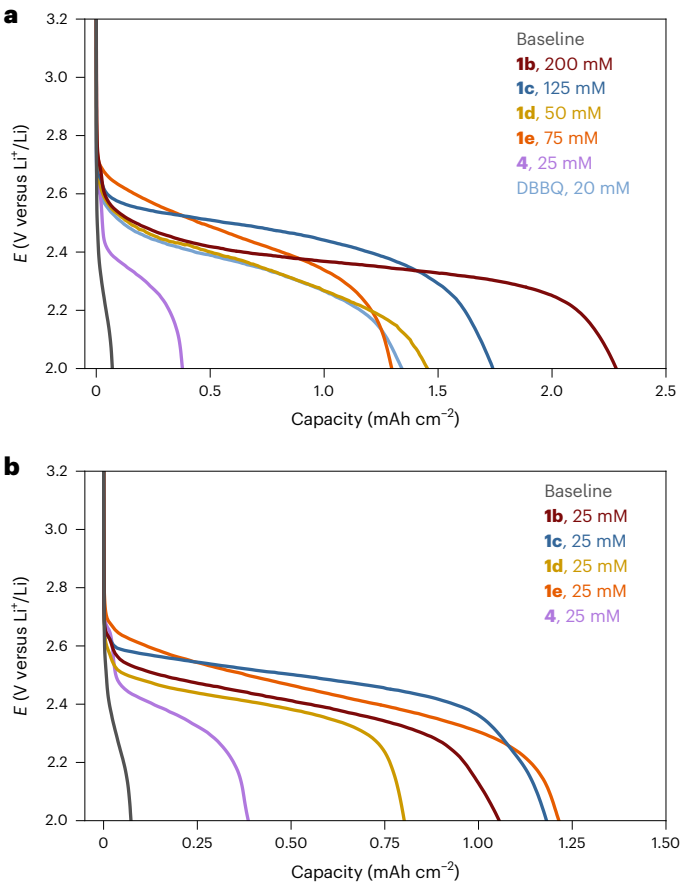

Fig. 4 | Battery discharge curves for Li–O_2 cells prepared with 1 M LiOTF in TEGDME and an LFP anode. a, Battery discharge curves for redox mediator solutions prepared at their maximum concentrations (**1b**, 200 mM; **1c**, 125 mM; **1d**, 50 mM; **1e**, 75 mM; **4**, 25 mM; DBBQ, 20 mM). **b**, Battery discharge curves for redox mediator solutions prepared at uniform, 25 mM concentrations. Both panels show the discharge curve from a baseline redox mediator-free cell (grey trace).

negative (Fig. 3). The trend in $\log(k_2)$ versus $E_{R^+/R\cdot}$ is consistent with the model for redox catalysis rate-controlled by the electron-transfer step (activation control)[43,44] reported by Savéant, so our data in Supplementary Fig. 8 were fit to the following expression:

$$\log(k_2) = \log(k_s) - \frac{\alpha}{0.058}\left(E_{R^+/R\cdot} - E_{O_2/O_2^-}\right) \quad (3)$$

where k_s is the solution electron exchange rate constant, α is 0.5 and E_{O_2/O_2^-} is 2.40 V. The fit provided a k_s value of 1.774×10^7 M^{-1} s^{-1}, which agrees well with other studies on outer-sphere redox mediators[43,44].

Two key conclusions were drawn from our CV analysis. First, the inner-sphere mechanism did not result in catalytic ORR for any R^+ derivatives investigated in this Article. Although some radicals react with O_2, the corresponding peroxides were inert toward Li^+ ions, preventing closure of the catalytic cycle. Although no R^+ derivatives showed inner-sphere catalysis, such a process can be achieved in other derivatives whose energetics are tuned to satisfy the energy landscape in Fig. 2b. Second, cations with $E_{R^+/R\cdot}$ in the 2.54–2.95 V range showed detectable catalytic enhancements via the outer-sphere mechanism, but only in the presence of Li^+, suggesting Li^+-coupled catalysis. Catalytic rate constants increased with thermodynamic driving force for electron transfer, as predicted by the Marcus electron transfer model[43,44].

Battery discharge

The influence of outer-sphere redox mediation on Li–O_2 discharge was evaluated as described in the Methods using either $LiFePO_4$ (LFP) or unprotected Li anodes. In the absence of redox mediators (Fig. 4, grey traces), the discharge quickly terminated at the 2.0 V cutoff potential after a capacity of 0.065 mAh cm^{-2} because of the surface-mediated O_2 reduction and carbon electrode passivation by a Li_2O_2 film[3]. Consistent with the redox mediation observed in CVs, the discharge capacity increased in the presence of redox mediators for both LFP (Fig. 4) and Li (Supplementary Fig. 9) anodes. However, the discharge capacities are larger for each redox mediator in LFP-containing cells, providing evidence that the reaction between R^+ and Li was consuming R^+ and effectively lowered their concentration. To further confirm the effect of outer-sphere redox mediation, differential electrochemical mass spectrometry (DEMS) measurements were carried out on Li–O_2 cells lacking redox mediators and containing **1c**. Average e^-/O_2 ratios of 2.53 and 2.16 were determined for the baseline and redox-mediated cells, respectively, suggesting that the predominant product in the redox-mediated cell was Li_2O_2.

Generally, the discharge capacities increased with R^+ concentration (Supplementary Figs. 10 and 11), probably due to the presence of two competing Li_2O_2 formation pathways: (1) a surface-mediated pathway, which results in passivating Li_2O_2 films on the electrode surface, and (2) the desired redox-mediated pathway, which moves Li_2O_2 formation into the solution phase. At higher R^+ concentrations, the redox-mediated process dominates, resulting in larger discharge capacities. Given these results, the performance of each mediator was evaluated at its solubility limit (Fig. 4a). The identity and morphology of the discharge product was determined using Raman spectroscopy, scanning electron microscopy (SEM) and UV–vis titration with $TiOSO_4$. Raman bands present at ~250 and 790 cm^{-1} (Supplementary Fig. 14) were attributed to the presence of Li_2O_2 as a discharge product, which was further confirmed by colorimetric titration with $TiOSO_4$ (Supplementary Table 5). The formed Li_2O_2 particles appear in SEM images as small flakes on the electrode surface (Supplementary Fig. 15), matching what has been observed previously for some quinone-based redox mediators[8].

Discharge plateaus of redox mediator-containing cells appear with lower overpotentials and tend to scale with $E_{R^+/R\cdot}$. They also achieved substantially larger discharge capacities, ranging from 6- to 35-fold, which was attributed to redox mediation moving the O_2/LiO_2 reduction into solution and mitigating surface-mediated reduction. The best performance was observed with **1b**, which provided capacities competitive with those reported for quinone-based and other mediators[6–22] (DBBQ[9] is shown in Fig. 4a). Outer-sphere redox mediation often generates reactive oxygen species that have detrimental effects on cell performance; however, this is not a concern in our work. First, Li^+-coupled oxygen reduction avoids O_2^- formation and instead generates LiO_2 intermediates that are non-parasitic in Li–O_2 cells[47]. Second, DEMS measurements suggest there is nearly no side-product formation during Li–O_2 cell discharge. These results provide encouraging evidence that the organic cations in Fig. 1 provide an important expansion of the library of functional redox mediators for Li–O_2 batteries.

A more quantitative comparison was made by testing the redox mediators at uniform concentrations of 25 mM (Fig. 4b). Surprisingly, the battery discharge capacity increased with more positive $E_{R^+/R\cdot}$, counter to the observed relationship between $E_{R^+/R\cdot}$ and $\log(k_2)$ in the CV section. Equation (3) predicts that redox mediation rates increase as the thermodynamic driving force for electron transfer between $R^\cdot$ and $Li^+\cdots O_2$ increases, that is, the more negative $E_{R^+/R\cdot}$, as expected for the normal Marcus region. Here, the opposite behaviour is observed. Results from our CV and chronopotentiometry measurements are compared in Fig. 5a, which shows how bimolecular rate constants k_2 (blue points) and battery discharge capacities (red bars) change as a function of $E_{R^+/R\cdot}$. Clearly, redox mediators which react more slowly

https://doi.org/10.1038/s41557-023-01268-0

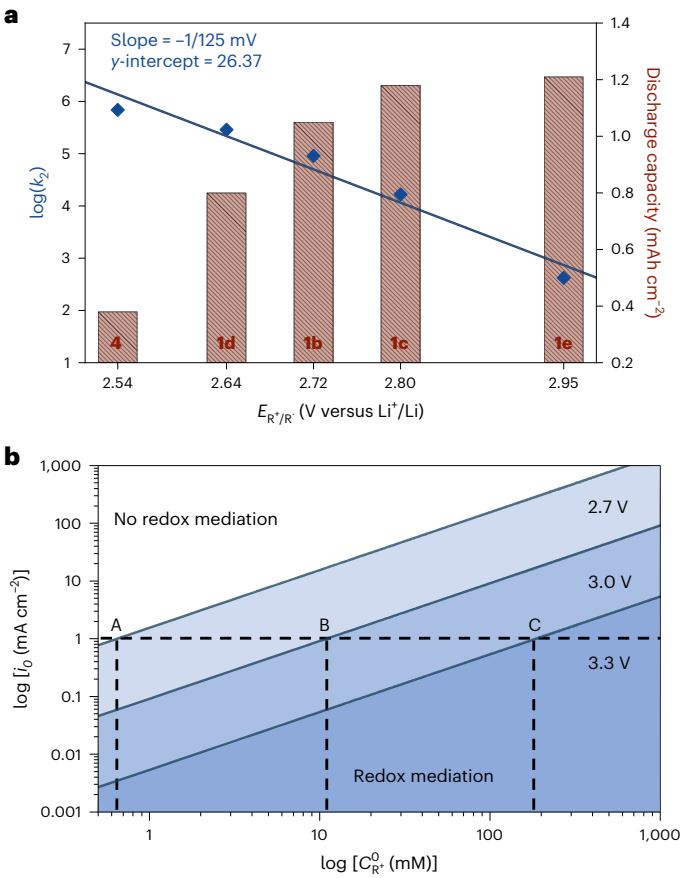

Fig. 5 | Correspondence of $E_{R^+/R^\cdot}$ and effective outer-sphere redox mediation. a, Plot of rate constants k_2 (blue points) and discharge capacities (red histogram) as a function of $E_{R^+/R^\cdot}$. Discharge capacities were obtained from data in Fig. 4b. **b**, Chronopotentiometry simulations showing catalytic (blue) and non-catalytic (white) regions for three specified $E_{R^+/R^\cdot}$ values ($E_{R^+/R^\cdot}$ = 2.7, 3.0 and 3.3 V) at a wide range of current densities (i_0) and R^+ concentrations ($C^0_{R^+}$). A single current density of 1 mA cm^{-2} is indicated by the horizontal dashed line, and where this line intersects the borders of the three shaded regions (A, B and C) determines the minimum R^+ concentration required for redox catalysis at a specified $E_{R^+/R^\cdot}$. Points A and C illustrate that, as $E_{R^+/R^\cdot}$ increases from 2.7 to 3.3 V, increasing R^+ concentrations (0.7 to 187 mM) are needed to maintain redox mediation conditions.

with $Li^+\cdots O_2$, yield larger discharge capacities. CV measurements probe the electrochemical processes that occur on short timescales, varying in the microseconds-to-seconds range, depending on sweep rate. As such, CV is an excellent tool to study electron-transfer kinetics, but battery capacity depends on chemical processes, such as Li_2O_2 crystal growth, which take place at timescales longer than the CV temporal window. The opposing trends displayed in Fig. 5a point to the dangers associated with relying solely on CV to screen for efficient redox mediators.

Notably, DBBQ diverges from our observed trends. DBBQ proceeds through an inner-sphere mechanism, forming a $Li\cdots DBBQ\cdots O_2$ adduct as a key intermediate, and imparting comparatively smaller bimolecular ORR rate constants (Supplementary Fig. 16)[9,46,48]. However, the discharge capacities of DBBQ-containing cells (1.33 mAh cm^{-2}) were larger than any of our redox mediators at similar concentrations (Supplementary Fig. 16). The inner-sphere pathway must increase the reduced oxygen intermediate lifetimes (for example, $Li\cdots DBBQ\cdots O_2$), giving more time for diffusion away from the electrode[15,49]. Although this is beneficial, we point out that our cationic outer-sphere redox mediators can be prepared at much larger concentrations than the quinone derivatives.

The trend observed in Fig. 5a can be explained by the competition between surface- and solution-mediated O_2/Li_2O_2 reduction processes. The surface-mediated process favours the formation of surface-adsorbed LiO_2 intermediates, which give way to insulating Li_2O_2 films and result in rapid cell termination[3]. The solution-mediated process favours soluble LiO_2 intermediates, which extend discharge capacities. The cell potential has a drastic effect on the competition between these processes, with the surface-mediated process being favoured at larger overpotentials[50]. Because the surface-mediated process is favoured at potentials near 2.5 V, as $E_{R^+/R^\cdot}$ values get nearer that potential, the redox mediator becomes less able to suppress the surface-mediated process. Such mediators could be made more competitive if their concentration is substantially higher than $Li^+\cdots O_2$. This avenue of research should be explored further. At the millimolar R^+ concentrations used in this study, both $Li^+\cdots O_2$ and R^+ species are available near the electrode surface, leading to competition between surface- and redox-mediated processes.

Given the relationship between discharge capacity and increasing $E_{R^+/R^\cdot}$ values, it is probable that further improvements are expected if redox mediators with more positive potentials are utilized. However, electron transfer between $R^\cdot$ and $Li^+\cdots O_2$ will become increasingly unfavourable as $E_{R^+/R^\cdot}$ increases, eventually leading to loss of activity. Increasing redox mediator concentration beyond standard conditions can overcome this: at high concentrations of electrochemically generated $R^\cdot$, electron transfer to $Li^+\cdots O_2$ will become thermodynamically favourable, even for highly positive $E_{R^+/R^\cdot}$ values, because of the equilibrium shift caused by Le Chatelier's principle. In other words, the reaction between $R^\cdot$ and O_2 can be made thermodynamically favourable even for $E_{R^+/R^\cdot}$ values above 2.96 V, as long as the $R^\cdot$ concentration is much higher than the R^+ concentration. High $R^\cdot$ concentrations in discharge experiments can be achieved by 'sacrificing' a fraction of current density for the conversion of R^+ to $R^\cdot$. In other words, such a process is not truly 'catalytic', because a large portion of $R^\cdot$ is never converted back to R^+. Instead, the excess $R^\cdot$ serves to generate the requisite driving force for electron transfer from $R^\cdot$ to O_2. Thus, a critical question remains: how positive can $E_{R^+/R^\cdot}$ be pushed and it still be able to mediate O_2 reduction? To determine this, the chronopotentiometric response was modelled based on redox-mediated O_2 reduction and is presented in Fig. 5b. Full discussion of the modelling can be found in the Methods and Supplementary Section 3. Shaded regions in Fig. 5b show the range of current densities (i_0) and R^+ concentrations ($C^0_{R^+}$) expected to yield effective redox mediation at specified $E_{R^+/R^\cdot}$ (2.7, 3.0 and 3.3 V). This model uncovers key guidelines for the discovery of future redox mediators: redox mediation can be achieved for a wide range of $E_{R^+/R^\cdot}$, even values of 3.0 V and above, as long as the R^+ concentrations can be increased enough to accommodate the chosen current density.

Conclusions

An unexplored class of triarylmethyl cation discharge redox mediators for Li–O_2 batteries has been investigated using computational and experimental approaches. Inner- and outer-sphere mechanisms were explored computationally, but experimental work shows only the outer-sphere mechanism results in closure of the catalytic cycle. The increased rate of reaction between R^+ and O_2 with more negative $E_{R^+/R^\cdot}$ values is indicative of outer-sphere redox mediation and Marcus-type rate dependence on the thermodynamic driving force. Enhancements to Li–O_2 discharge capacity rivalling those of well-studied quinone-based mediators were realized, revealing a class of molecular motifs whose derivatives can be explored as future redox mediators. Comparative CV and chronopotentiometric studies resulted in an interesting finding: improved discharge capacities were obtained for kinetically 'sluggish' redox mediators. More specifically, a clear

relationship between discharge capacity and more positive $E_{R^+/R}$ values was observed, which underscores the importance of controlling discharge potential to improve capacity. The observed behaviour is explained by competition between surface-mediated and redox-mediated oxygen reduction, with the surface-mediated process being less efficient as the cell potential becomes more positive. Chronopotentiometry simulations revealed that redox mediation can be achieved for $E_{R^+/R}$ values as positive as 2.96 V, but they must be operated at high concentrations to enable spontaneous electron transfer to O_2. Based on the desire to reduce the discharge overpotential and prolong battery discharge times, this finding will be instrumental for the discovery of future redox mediators with more positive reduction potentials that may be prepared at high concentrations.

Online content

Any methods, additional references, Nature Portfolio reporting summaries, source data, extended data, supplementary information, acknowledgements, peer review information; details of author contributions and competing interests; and statements of data and code availability are available at https://doi.org/10.1038/s41557-023-01268-0.

References

1. Kwak, W.-J. et al. Lithium-oxygen batteries and related systems: potential, status and future. *Chem. Rev.* **120**, 6626–6683 (2020).
2. Aurbach, D., McCloskey, B. D., Nazar, L. F. & Bruce, P. G. Advances in understanding mechanisms underpinning lithium–air batteries. *Nat. Energy* **1**, 16128 (2016).
3. Viswanathan, V. et al. Electrical conductivity in Li_2O_2 and its role in determining capacity limitations in non-aqueous Li-O_2 batteries. *J. Chem. Phys.* **135**, 214704 (2011).
4. Aetukuri, N. B. et al. Solvating additives drive solution-mediated electrochemistry and enhance toroid growth in non-aqueous Li–O_2 batteries. *Nat. Chem.* **7**, 50–56 (2015).
5. Burke, C. M., Pande, V., Khetan, A., Viswanathan, V. & McCloskey, B. D. Enhancing electrochemical intermediate solvation through electrolyte anion selection to increase nonaqueous Li-O_2 battery capacity. *Proc. Natl Acad. Sci. USA* **112**, 9293–9298 (2015).
6. Zhang, Y. et al. Potential-dependent generation of O_2^- and LiO_2 and their critical roles in O_2 reduction to Li_2O_2 in aprotic Li-O_2 batteries. *J. Phys. Chem. C* **120**, 3690–3698 (2016).
7. Dai, A., Li, Q., Liu, T., Amine, K. & Lu, J. Fundamental understanding of water-induced mechanisms in Li-O_2 batteries: recent developments and perspectives. *Adv. Mater.* **31**, 1805602 (2019).
8. Han, X.-B. & Ye, S. Structural design of oxygen reduction redox mediators (ORRMs) based on anthraquinone (AQ) for the Li-O_2 battery. *ACS Catal.* **10**, 9790–9803 (2020).
9. Gao, X., Chen, Y., Johnson, L. & Bruce, P. G. Erratum: promoting solution phase discharge in Li–O_2 batteries containing weakly solvating electrolyte solutions. *Nat. Mater.* **15**, 918 (2016).
10. Matsuda, S., Hashimoto, K. & Nakanishi, S. Efficient Li_2O_2 formation via aprotic oxygen reduction reaction mediated by quinone derivatives. *J. Phys. Chem. C* **118**, 18397–18400 (2014).
11. Sun, D. et al. A solution-phase bifunctional catalyst for lithium-oxygen batteries. *J. Am. Chem. Soc.* **136**, 8941–8946 (2014).
12. Zhang, Y. et al. High-capacity and high-rate discharging of a coenzyme Q_{10}-catalyzed Li-O_2 battery. *Adv. Mater.* **30**, 1705571 (2018).
13. Ko, Y. et al. Biological redox mediation in electron transport chain of bacteria for oxygen reduction reaction catalysts in lithium-oxygen batteries. *Adv. Funct. Mater.* **29**, 1805623 (2019).
14. Lacey, M. J., Frith, J. T. & Owen, J. R. A redox shuttle to facilitate oxygen reduction in the lithium air battery. *Electrochem. Commun.* **26**, 74–76 (2013).
15. Yang, L., Frith, J. T., Garcia-Araez, N. & Owen, J. R. A new method to prevent degradation of lithium-oxygen batteries: reduction of superoxide by viologen. *Chem. Commun.* **51**, 1705–1708 (2015).
16. Hwang, C. et al. Biomimetic superoxide disproportionation catalyst for anti-aging lithium-oxygen batteries. *ACS Nano* **13**, 9190–9197 (2019).
17. Lee, D. et al. Direct observation of redox mediator-assisted solution-phase discharging of Li-O_2 battery by liquid-phase transmission electron microscopy. *J. Am. Chem. Soc.* **141**, 8047–8052 (2019).
18. Kwak, W.-J. et al. Understanding the behavior of Li-oxygen cells containing LiI. *J. Mater. Chem. A* **3**, 8855–8864 (2015).
19. Kwak, W.-J. et al. Li-O_2 cells with LiBr as an electrolyte and a redox mediator. *Energy Environ. Sci.* **9**, 2334–2345 (2016).
20. Sharon, D. et al. Catalytic behavior of lithium nitrate in Li-O_2 cells. *ACS Appl. Mater. Interfaces* **7**, 16590–16600 (2015).
21. Liu, T. et al. Cycling Li-O_2 batteries via LiOH formation and decomposition. *Science* **350**, 530–533 (2015).
22. Yang, H., Wang, Q., Zhang, R., Trimm, B. D. & Whittingham, M. S. The electrochemical behaviour of TTF in Li-O_2 batteries using a TEGDME-based electrolyte. *Chem. Commun.* **52**, 7580–7583 (2016).
23. Bergner, B. J., Schürmann, A., Peppler, K., Garsuch, A. & Janek, J. TEMPO: a mobile catalyst for rechargeable Li-O_2 batteries. *J. Am. Chem. Soc.* **136**, 15054–15064 (2014).
24. Lim, H.-D. et al. Rational design of redox mediators for advanced Li–O_2 batteries. *Nat. Energy* **1**, 16066 (2016).
25. Zhang, C. et al. A comparative study of redox mediators for improved performance of Li-oxygen batteries. *Adv. Energy Mater.* **10**, 2000201 (2020).
26. Gao, X., Chen, Y., Johnson, L. R., Jovanov, Z. P. & Bruce, P. G. A rechargeable lithium–oxygen battery with dual mediators stabilizing the carbon cathode. *Nat. Energy* **2**, 17118 (2017).
27. Weerasooriya, R. B. et al. Kinetics of hydride transfer from catalytic metal-free hydride donors to CO_2. *J. Phys. Chem. Lett.* **12**, 2306–2311 (2021).
28. Lim, C.-H. et al. Benzimidazoles as metal-free and recyclable hydrides for CO_2 reduction to formate. *J. Am. Chem. Soc.* **141**, 272–280 (2019).
29. Zoric, M. R., Kadel, U. P. & Glusac, K. D. Cocatalysis: role of organic cations in oxygen evolution reaction on oxide electrodes. *ACS Appl. Mater. Interfaces* **10**, 26825–26829 (2018).
30. Ilic, S., Pandey Kadel, U., Basdogan, Y., Keith, J. A. & Glusac, K. D. Thermodynamic hydricities of biomimetic organic hydride donors. *J. Am. Chem. Soc.* **140**, 4569–4579 (2018).
31. Ilic, S., Alherz, A., Musgrave, C. B. & Glusac, K. D. Thermodynamic and kinetic hydricities of metal-free hydrides. *Chem. Soc. Rev.* **47**, 2809–2836 (2018).
32. Yang, X. et al. Mechanistic studies of electrode-assisted catalytic oxidation by flavinium and acridinium cations. *ACS Catal.* **4**, 2635–2644 (2014).
33. Zoric, M. R. et al. Conformational flexibility of xanthene-based covalently linked dimers. *J. Phys. Org. Chem.* **29**, 505–513 (2016).
34. Mirzakulova, E. et al. Electrode-assisted catalytic water oxidation by a flavin derivative. *Nat. Chem.* **4**, 794–801 (2012).
35. Ilic, S., Alherz, A., Musgrave, C. B. & Glusac, K. D. Importance of proton-coupled electron transfer in cathodic regeneration of organic hydrides. *Chem. Commun.* **55**, 5583–5586 (2019).
36. Hogan, D. T. & Sutherland, T. C. Modern spin on the electrochemical persistence of heteroatom-bridged triphenylmethyl-type radicals. *J. Phys. Chem. Lett.* **9**, 2825–2829 (2018).
37. Erabi, T., Asahara, M., Miyamoto, M., Goto, K. & Wada, M. 9-Phenylxanthen-9-ylium and 9-phenylthioxanthen-9-ylium ions: comparison of *o*- and *p*-substitutions in the 9-phenyl group by cyclic voltammetry and visible spectra. *Bull. Chem. Soc. Jpn* **75**, 1325–1332 (2002).

38. Ilic, S., Brown, E. S., Xie, Y., Maldonado, S. & Glusac, K. D. Sensitization of p-GaP with monocationic dyes: the effect of dye excited-state lifetime on hole injection efficiencies. *J. Phys. Chem. C* **120**, 3145–3155 (2016).
39. Hapiot, P., Moiroux, J. & Saveant, J. M. Electrochemistry of NADH/NAD^+ analogs. A detailed mechanistic kinetic and thermodynamic analysis of the 10-methylacridan/10-methylacridinium couple in acetonitrile. *J. Am. Chem. Soc.* **112**, 1337–1343 (1990).
40. Gostowski, R. C., Bailey, T., Bonner, S. D., Emrich, E. E. & Steelman, S. L. Steric hindrance effects on bimolecular coupling rate constants of carbon-centered radicals. *J. Phys. Org. Chem.* **13**, 735–739 (2000).
41. Chase, M. W. NIST-JANAF thermochemical tables. *J. Phys. Chem. Ref. Data* **9**, 1510 (1998).
42. Vasudevan, D. & Wendt, H. Electroreduction of oxygen in aprotic media. *J. Electroanal. Chem.* **392**, 69–74 (1995).
43. Andrieux, C. P., Dumas-Bouchiat, J. M. & Saveant, J. M. Homogeneous redox catalysis of electrochemical reactions: Part I. Introduction. *J. Electroanal. Chem. Interfacial Electrochem.* **87**, 39–53 (1978).
44. Andrieux, C. P., Blocman, C., Dumas-Bouchiat, J. M. & Saveant, J. M. Heterogeneous and homogeneous electron transfers to aromatic halides. An electrochemical redox catalysis study in the halobenzene and halopyridine series. *J. Am. Chem. Soc.* **101**, 3431–3441 (1979).
45. Andrieux, C. P., Hapiot, P. & Sa Véant, J. M. Electron transfer coupling of diffusional pathways. Homogeneous redox catalysis of dioxygen reduction by the methylviologen cation radical in acidic dimethylsulfoxide. *J. Electroanal. Chem. Interfacial Electrochem.* **189**, 121–133 (1985).
46. Bawol, P. P., Thimm, J. H. & Baltruschat, H. Unraveling the mechanism of the solution-mediated oxygen reduction in metal-O_2 batteries: the importance of ion association. *ChemElectroChem* **6**, 6038–6049 (2019).
47. Lu, J. et al. A lithium–oxygen battery based on lithium superoxide. *Nature* **529**, 377–382 (2016).
48. Wu, S. et al. Revealing the catalytic pathway of a quinone-mediated oxygen reduction reaction in aprotic Li-O_2 batteries. *Chem. Commun.* **58**, 1025–1028 (2022).
49. Zhu, Y. G. et al. Synergistic oxygen reduction of dual redox catalysts boosting the power of lithium-air battery. *Phys. Chem. Chem. Phys.* **20**, 27930–27936 (2018).
50. Kwabi, D. G. et al. Controlling solution-mediated reaction mechanisms of oxygen reduction using potential and solvent for aprotic lithium-oxygen batteries. *J. Phys. Chem. Lett.* **7**, 1204–1212 (2016).

Methods

Synthesis

Unless otherwise specified, reagents were procured from commercial sources and used as received. ^{1}H NMR spectra were collected using a Bruker DPX spectrometer operating at 9.4 T (400 MHz) or a Bruker Avance III HD spectrometer operating at 11.74 T (500 MHz). 2,7-Dimethyl-9-mesityl-10-methylacridinium tetrafluoroborate (**1b**), 9-mesityl-10-methylacridinium tetrafluoroborate (**1c**) and DBBQ were purchased from Millipore-Sigma and 2,7-difluoro-9-mesityl-10-methylacridinium tetrafluoroborate (**1e**) from AmBeed.

Phenylmagnesium bromide synthesis

Phenylmagnesium bromide (Grignard) reagents were made on demand for specific redox mediator synthesis. In a dry flask attached to a Schlenk line, with a dry stir bar, 1 equiv. of dried Mg powder and a few small crystals of I_2 were added and the headspace was purged with Ar gas. One equivalent of bromobenzene dissolved in dry tetrahydrofuran (THF; 20 ml) was added to the Mg powder. The solution was briefly heated to begin the reaction and then placed in an ambient-temperature water bath. The reaction mixture was then stirred for 60 min. Once completed, the crude Grignard reagent was used without isolation for subsequent steps.

9-phenyl-10-methylacridinium triflate (1a)

1a was made by a modified procedure taken from the literature[36]. First the acridinol analogue (9-phenyl-10-methylacridin-9-ol) was made by first dissolving 10-methylacridinone (0.50 g, 2.39 mmol, 1 equiv.) in dry THF (50 ml), then the 10-methylacridinone was added dropwise to an Ar-purged, phenylmagnesium bromide-containing (2.2 equiv.) Schlenk flask over a 20-min period. The flask was chilled to 0 °C in an ice bath during 10-methylacridinone addition, then allowed to warm to room temperature and stirred for 24 h. The reaction was quenched with aqueous NH_4Cl (10 ml) and diluted with ethyl acetate (EtOAc) and H_2O. The aqueous layer was extracted with EtOAc three times. The resulting organic layer was dried over anhydrous $MgSO_4$. The solvent was evaporated, yielding a solid white product that matched the published spectrum[36].

To make **1a**, 9-phenyl-10-methylacridin-9-ol (0.25 g, 0.87 mmol) and a magnetic stir bar were added to a dry 15-ml vial that was purged with Ar. The 9-phenyl-10-methylacridin-9-ol was dissolved under stirring in dry Et_2O at room temperature. Triflic acid (0.082 ml, 0.97 mmol, 1.1 equiv.) was added to the vial and the mixture was stirred for an additional 30 min and then chilled to 0 °C. The precipitate was filtered, washed with anhydrous Et_2O and dried in vacuum to give a solid product. The ^{1}H NMR spectrum of **1a** matched the previously published spectrum[36].

9-(2,6-dimethoxyphenyl)-1,8-dimethoxy-10-methyacridinium perchlorate (1d)

1d was synthesized by a modified procedure from the literature[38]. First, the precursor tris(2,6-dimethoxyphenyl)methylium perchlorate was made. 1,3-Dimethoxybenzene (2 ml, 15.4 mmol, 3.5 equiv.) was dissolved in dry THF (10 ml) under argon, then 2.5 M *n*-butyl lithium in hexane (6.2 ml, 15.4 mmol, 3.5 equiv.) was added dropwise at −78 °C. After 30 min, the solution was warmed to room temperature and stirred for 1 h. Diethyl carbonate (0.52 ml, 4.4 mmol, 1 equiv.), dissolved in 25 ml of benzene, was added to the solution, which was stirred and refluxed for two days. The reaction was quenched in water and extracted with dichloromethane. Combined CH_2Cl_2 layers were added, dried, and the solvent was evaporated, yielding a brownish residue. The product was dissolved in acetonitrile, perchloric acid was added, and a precipitate formed. The precipitate was collected, washed with Et_2O, and dried under vacuum. The ^{1}H NMR spectrum matched the published spectrum[38].

To make **1d**, tris(2,6-dimethoxyphenyl)methylium perchlorate (1 g, 2 mmol) was dissolved in 15 ml of *N*-methylpyrrolidine to which 1.2 ml of methylamine (33% in ethanol, 9.6 mmol, 4.8 equiv.) was added. The mixture was stirred for 12 h, then poured into Et_2O under stirring. The red precipitate was collected, washed with Et_2O and dried under vacuum. The ^{1}H NMR spectrum of **1d** matched the published spectrum[38].

9-phenylxanthylium triflate (2a)

2a was synthesized by a modified procedure from the literature[36]. First, the xanthenol analogue (9-phenyl-xanthen-9-ol) was made as follows: xanthone (0.50 g, 2.54 mmol, 1 equiv.) was dissolved in dry THF (50 ml), then the xanthone was added dropwise to an Ar-purged, phenylmagnesium bromide-containing (2.2 equiv.) Schlenk flask over a 20-min period. The flask was chilled to 0 °C in an ice bath during xanthone addition, then allowed to warm to room temperature and stirred for 24 h. The reaction was quenched with aqueous NH_4Cl (10 ml) and diluted with EtOAc and H_2O. The aqueous layer was extracted with EtOAc three times. The resulting organic layer was dried over anhydrous $MgSO_4$. The solvent was evaporated, yielding a solid white product that matched the published spectrum[36].

To make **2a**, 9-phenyl-xanthen-9-ol (0.25 g, 0.91 mmol, 1 equiv.) and a magnetic stir bar were added to a dry 15-ml vial that was purged with Ar, then the 9-phenyl-xanthen-9-ol was dissolved under stirring in dry Et_2O at room temperature. Triflic acid (0.085 ml, 1.00 mmol, 1.1 equiv.) was added to the vial, and the mixture was stirred for an additional 30 min, then chilled to 0 °C. The precipitate was filtered, washed with anhydrous Et_2O and dried in vacuum to give solid product. The ^{1}H NMR spectrum of **2a** matched the previously published spectrum[36].

9-(4-tolyl)xanthylium perchlorate (2b)

2b was synthesized by a modified procedure from the literature[37]. First, the xanthenol analogue, 9-(4-tolyl)-9*H*-xanthen-9-ol was made as follows: 1,3,5-trimethylbenzene (72 mg, 0.6 mmol) was dissolved in 1.3 ml of dry THF, and the solution was purged with Ar, then *n*-butyl lithium (0.6 mmol, 0.24 ml, 2.5 M) was added to the mixture dropwise at −78 °C. The resultant mixture was warmed to room temperature and stirred under Ar for 2 h. The mixture was cooled to 0 °C and xanthone (0.1167 g, 0.6 mmol) dissolved in a minimal amount of toluene was added to the solution. The mixture was stirred for 24 h and allowed to warm to room temperature during that time. The reaction was quenched with water and the product was extracted with dichloromethane. Combined CH_2Cl_2 layers were added and dried over anhydrous $MgSO_4$. The solvent was evaporated and yielded a white solid product. The ^{1}H NMR spectrum of 9-(4-tolyl)-9*H*-xanthen-9-ol matched the already published spectrum[37].

To make **2b**, a 15-ml vial was charged with 9-(4-tolyl)-9*H*-xanthen-9-ol (0.50 mmol) and concentrated perchloric acid (70%, 4 ml). The resulting mixture was stirred overnight. The precipitate was filtered off, washed with anhydrous diethyl ether (Et_2O, 15 ml), and dried in vacuum to give a solid product. The ^{1}H NMR spectrum matched the previously published spectrum[37].

9-(2,4,6-trimethoxyphenyl)xanthylium perchlorate (2c)

2c was synthesized by a modified procedure from the literature[37]. First, the xanthenol analogue, 9-(2,4,6-trimethoxy)-9*H*-xanthen-9-ol was made as follows: 1,3,5-trimethoxybenzene (100 mg, 0.6 mmol) was dissolved in 1.3 ml of dry THF and the solution was purged with Ar, then *n*-butyl lithium (0.6 mmol, 0.24 ml, 2.5 M) was added to the reaction mixture dropwise via canula at −78 °C. The reaction mixture was allowed to warm to room temperature and stirred under Ar for 2 h. The mixture was cooled to 0 °C and xanthone (0.1167 g, 0.6 mmol) dissolved in a minimal amount of toluene was added to the solution. The mixture was stirred for 24 h and allowed to warm to room temperature during that time. The reaction was quenched with water followed by extraction with CH_2Cl_2. Organic layers were merged and dried over anhydrous magnesium sulfate. After the CH_2Cl_2 was evaporated, it yielded a white

solid. The ^{1}H NMR spectrum of 9-(2,4,6-trimethoxy)-9*H*-xanthen-9-ol matched the already published spectrum[37].

To make **2c**, a 15-ml vial was charged with 9-(2,4,6-trimethoxy)-9*H*-xanthen-9-ol (0.50 mmol) and concentrated perchloric acid (70%, 4 ml). The resulting mixture was stirred overnight. The precipitate that formed was filtered off, washed with anhydrous Et_2O (15 ml), and dried in vacuum to give a solid product. The ^{1}H NMR spectrum matched the previously published spectrum[37].

1,13-dimethoxy-5,9-dimethyl-5,9-dihydro-13*bH*-quinolino[2,3,4-*kl*]acridinium perchlorate (4)

4 was synthesized by a modified procedure from the literature[38]. **1d** (200 mg, 0.51 mmol, 1 equiv.) was dissolved in 10 ml of *N*-methylpyrrolidine, then 2.6 ml of methylamine solution in ethanol (33%, 13.3 mmol, 26 equiv.) was added and the mixture was stirred at 90 °C for 8 h under ambient conditions. The reaction was allowed to cool and was poured into a cooled 50% aqueous solution of $HClO_4$. This formed a dark green precipitate, which was filtered, washed with Et_2O and dried under vacuum. The ^{1}H NMR spectrum of **4** matched the published spectrum[38].

4,8,12-trimethyl-4,8,12-triazatriangulenium perchlorate (5)

5 was synthesized by a modified procedure from the literature[51]. **4** (100 mg, 0.24 mmol) was dissolved in 10 ml of *N*-methylpyrrolidine, then 1.2 ml of methylamine solution in ethanol (33%, 6.2 mmol, 26 equiv.) was added and the mixture was stirred at 90 °C for 8 h under ambient conditions. The reaction was allowed to cool and was poured into a cooled 50% aqueous solution of $HClO_4$. The precipitate was filtered, washed with Et_2O and dried under vacuum. The ^{1}H NMR spectrum of **5** matched the published spectrum[51].

Chemically derived peroxide 9-phenylxanthyl peroxide (**2a**/RO–OR) was prepared according to published procedures[37] and its putative structure is reported in Supplementary Section 1. ^{1}H NMR ($(CD_3)_2CO$, 500 MHz): 7.37 (4*H*, t), 7.23–7.13 (10*H*, m), 7.00–6.93 (8*H*, m), 6.74 (4*H*, d).

Chemically derived peroxide 9-(4-tolyl)xanthyl peroxide **2b** (**2b**/RO–OR) was prepared according to published procedures[37] and its putative structure is reported in Supplementary Section 1. ^{1}H NMR ($(CD_3)_2CO$, 500 MHz): 7.35 (4*H*, t), 7.19 (4*H*, d), 6.99 (4*H*, d), 6.96 (4*H*, t), 6.84 (4*H*, d), 6.75 (4*H*, d), 3.76 (6*H*, s).

Electrochemically derived peroxide derivatives (**2a**/RO–OR and **2b**/RO–OR) were prepared and collected through amperostatic coulometry. In O_2-saturated solutions of **2a** and **2b**, a constant current (50 µA) was applied to the cell for 10-s intervals, and the solid was collected from the glassy carbon (GC) electrode and dissolved in THF. The electrochemically derived **2a**/RO–OR and **2b**/RO–OR showed the same NMR peaks as their chemically derived counterparts.

Electrochemistry

Tetrabutylammonium perchlorate was recrystallized from methanol. Lithium triflate (LiOTF) was dried under vacuum at 80 °C for three days before use. TEGDME was purchased from Millipore-Sigma and dried over 3-Å activated molecular sieves before use. The final water content of TEGDME was <100 ppm as measured by Karl Fischer titration. CV measurements were performed with a standard three-electrode set up with GC, 10 mM $Ag/AgNO_3$ and a Pt wire serving as the working, reference and counter electrodes, respectively. A Gamry 1010B potentiostat was used for CV measurements.

CV

All CV measurements were performed in a three-electrode cell set-up using GC (MF-2012, Bioanalytical systems, 0.075-cm^2 surface area), 10 mM $Ag/AgNO_3$ non-aqueous reference electrode (MF-2062, Bioanalytical systems) and Pt wire counter electrode (MW-4130 or MW-1033, Bioanalytical systems) and a Gamry 1010B potentiostat. Working electrodes were polished before each individual CV using alumina (CF-1050, Bioanalytical systems) and diamond (MF-2054, Bioanalytical systems) slurry polishes. CV experiments were conducted in dry TEGDME containing 1 M LiOTF and 3 mM redox mediator. For O_2-free and O_2-saturated measurements, solutions were purged for 20 min with Ar or O_2 gas, respectively. [O_2] in CV solutions was measured using a Neo-FoxGT O_2 sensor provided by Ocean Insight.

Battery testing

Swagelok Li–O_2 cells were assembled in an Ar-filled (MBraun) glovebox with H_2O and O_2 levels below 0.1 and 3 ppm, respectively, similar to previous descriptions[9]. Carbon gas diffusion layers (GDLs) were Freudenberg H23C2 GDLs and were provided by the Fuel Cell Store. For moisture removal, GDLs were dried under vacuum at 150 °C for three days before storage in a glovebox. During assembly, an LFP (3.5 V)[52] or Li metal anode was separated from a single, 5.6-mm diameter GDL disk by a Whatman glass-fibre paper separator. Redox mediator-containing, 1 M LiOTF TEGDME electrolyte (~0.150 ml) was added to the cathode side, and a stainless-steel-mesh current collector was used to cover the GDL. The assembled cells were placed inside hermetically sealed glass tubes, purged with dry O_2 and discharged on a Maccor battery cycler.

After discharge, the Swagelok Li–O_2 cells were disassembled to recover the carbon GDLs. The GDLs were washed with a small amount of dimethoxyethane and dried on a hot plate in the glovebox. After drying, the GDLs, deposits and films were characterized by SEM and Raman spectroscopy.

DEMS

DEMS measurements were performed according to a previously established method[47,53]. In short, a DEMS cell (MTI Corp) was assembled, using the same LFP anode, glass-fibre separator and carbon GDL as used in Swagelok-cell testing, inside the glovebox, and connected to the DEMS device. Once connected, the DEMS cell was purged with O_2 gas to ~20 p.s.i. and allowed to rest at open-circuit potential for 1 h. The overall cell volume was calibrated using a previously specified volume exchange technique[47,53]. The assembled cell volume was calibrated by replacement with five different standard volume loops (50, 100, 250, 500 and 1,000 µl) and comparing the partial pressure change within the cell. The overall volume was determined to be 6 ml. During discharge, the pressure inside the cell volume, and thus consumption of O_2, was monitored by an in-line pressure transducer. Oxygen consumption was compared to the discharge current to determine the mol e^- consumed per mol O_2.

Li_2O_2 quantification

Li_2O_2 quantification was performed using a previously reported UV–vis method[9,54]. In brief, the Li–O_2 cell was deconstructed and a glass-fibre separator and GDL were added to a small vial with 5 ml of $TiOSO_4$ in aqueous H_2SO_4. Li_2O_2 is known to spontaneously react with water to form H_2O_2 and, in the presence of $TiOSO_4$, a yellowish $[Ti(O_2)]^{2+}$ complex is formed with absorption at 410 nm. A small quantity of each solution was tenfold diluted to generate appropriate UV–vis solutions, which were compared with a calibration curve made with commercial Li_2O_2 (Aldrich).

Raman spectroscopy

Raman spectroscopy of the GDLs and their discharge products was performed with a Renishaw inVia Reflex microscope using either 633-nm (red) or 532-nm (green) laser light at the Electron Microscopy Core (EMC) at UIC's Research Resources Center (RRC). Inside the glovebox, the GDLs were loaded into an air-sensitive Raman cell with a thin quartz glass window for observation.

SEM imaging

SEM characterization was carried out using a JEOL JSM-IT500HR SEM in field-emission mode that is part of the EMC at the UIC RRC. Cleaned and dried GDLs were removed from the Ar glovebox in tightly sealed vials

and transferred as quickly as possible to the SEM vacuum chamber to minimize air exposure. All images were taken at ×6,000 magnification using a 5-keV acceleration voltage.

DFT calculations

All calculations were performed on Gaussian 09 or 16[55] software using the computational resources from the Laboratory Computing Resource Center at Argonne National Laboratory. Gas-phase optimization was performed using the B3LYP or uB3LYP hybrid functional[56,57] and 6–311g(d)[58] basis set. Single-point energies were calculated at the same level of theory using Et_2O solvation as implemented in the IEFPCM model[59]. Vibrational frequency analysis showed the presence of no imaginary frequencies in our optimized structures. Detailed information on the evaluation of each step in the catalytic mechanism is provided in Supplementary Section 2.

Chronopotentiometry modelling

Chronopotentiometry simulations were performed using a model involving electron transfer and a follow-up chemical step, as defined by equations (1) and (2), which has been defined previously[60]. Full details on the modelling are available in Supplementary Section 3.

Data availability

Source data for figures in the main text have been uploaded to the Figshare public data repository and can be accessed at https://doi.org/10.6084/m9.figshare.21719882 (ref. 61). Source data are provided with this paper.

Code availability

All computer codes used in this manuscript are available from the cited references.

References

51. Laursen, B. W. & Krebs, F. C. Synthesis of a triazatriangulenium salt. *Angew. Chem. Int. Ed.* **39**, 3432–3434 (2000).
52. Padhi, A. K., Nanjundaswamy, K. S. & Goodenough, J. B. Phospho-olivines as positive-electrode materials for rechargeable lithium batteries. *J. Electrochem. Soc.* **144**, 1188 (1997).
53. McCloskey, B. D., Bethune, D. S., Shelby, R. M., Girishkumar, G. & Luntz, A. C. Solvents' critical role in nonaqueous lithium-oxygen battery electrochemistry. *J. Phys. Chem. Lett.* **2**, 1161–1166 (2011).
54. Hartmann, P. et al. A comprehensive study on the cell chemistry of the sodium superoxide (NaO_2) battery. *Phys. Chem. Chem. Phys.* **15**, 11661–11672 (2013).
55. Frisch, M. J., Trucks, G. W., Schlegel, H. B., Scuseria, G. E. & Robb, M. A. Gaussian 09, Revision A.02 (Gaussian, 2016).
56. Becke, A. D. Density-functional exchange-energy approximation with correct asymptotic behavior. *Phys. Rev. A* **38**, 3098–3100 (1988).
57. Lee, C., Yang, W. & Parr, R. G. Development of the Colle-Salvetti correlation-energy formula into a functional of the electron density. *Phys. Rev. B* **37**, 785–789 (1988).
58. McLean, A. D. & Chandler, G. S. Contracted Gaussian basis sets for molecular calculations. I. Second row atoms, Z=11–18. *J. Chem. Phys.* **72**, 5639–5648 (1980).
59. Tomasi, J. & Persico, M. Molecular interactions in solution: an overview of methods based on continuous distributions of the solvent. *Chem. Rev.* **94**, 2027–2094 (1994).
60. Delahay, P., Mattax, C. C. & Berzins, T. Theory of voltammetry at constant current. IV. Electron transfer followed by chemical reaction. *J. Am. Chem. Soc.* **76**, 5319–5324 (1954).
61. Askins, E. J. et al. Triarylmethyl cation redox mediators enhance Li-O_2 battery discharge capacities. figshare https://doi.org/10.6084/m9.figshare.21719882 (2023).

Acknowledgements

K.D.G. acknowledges the support of the National Science Foundation and grant NSF 1954298. K.A. and L.A.C. thank the US Department of Energy for support under contract no. DE-AC02-06CH11357 from the Vehicle Technologies Office, which helped support the work done at ANL. We gratefully acknowledge the computing resources provided on Bebop, a high-performance computing cluster operated by the Laboratory Computing Resource Center (LCRC) at ANL. We also acknowledge the Electron Microscopy Core (EMC) at UIC's Research Resource's Center (RRC), where a substantial amount of post-discharge characterization was performed.

Author contributions

E.J.A., M.R.Z., R.A., K.A. and K.D.G. helped with the conception of this manuscript. E.J.A., M.R.Z. and L.A.C. performed the DFT evaluations and analysis of redox mediators. E.J.A. performed the CV experiments and analysis. E.J.A. performed the battery discharge experiments and analysis. E.J.A. and R.A. performed the post-discharge product characterization. E.J.A. and M.L. performed the DEMS experiments and analysis. E.J.A. and K.D.G. analysed crucial data and wrote the manuscript.

Competing interests

The authors declare no competing interests.

Additional information

Supplementary information The online version contains supplementary material available at https://doi.org/10.1038/s41557-023-01268-0.

Correspondence and requests for materials should be addressed to Ksenija D. Glusac.

Peer review information *Nature Chemistry* thanks Javier Carrasco, Kisuk Kang and the other, anonymous, reviewer(s) for their contribution to the peer review of this work.